





OPEN

Functionalization of eggshell membranes with CuO–ZnO based p–n junctions for visible light induced antibacterial activity against *Escherichia coli*

Nicoleta Preda^{1,4}, Andreea Costas^{1,4}, Mihaela Beregoi^{1,4}, Nicoleta Apostol¹, Andrei Kuncser¹, Carmen Curutiu², Florin Iordache³ & Ionut Enculescu¹

Biopolymers provide versatile platforms for designing naturally-derived wound care dressings through eco-friendly pathways. Eggshell membrane (ESM), a widely available, biocompatible biopolymer based structure features a unique 3D porous interwoven fibrous protein network. The ESM was functionalized with inorganic compounds (Ag, ZnO, CuO used either separately or combined) using a straightforward deposition technique namely radio frequency magnetron sputtering. The functionalized ESMs were characterized from morphological, structural, compositional, surface chemistry, optical, cytotoxicity and antibacterial point of view. It was emphasized that functionalization with a combination of metal oxides and exposure to visible light results in a highly efficient antibacterial activity against *Escherichia coli* when compared to the activity of individual metal oxide components. It is assumed that this is possible due to the fact that an axial p–n junction is created by joining the two metal oxides. This structure separates into components the charge carrier pairs promoted by visible light irradiation that further can influence the generation of reactive oxygen species which ultimately are responsible for the bactericide effect. This study proves that, by employing inexpensive and environmentally friendly materials (ESM and metal oxides) and fabrication techniques (radio frequency magnetron sputtering), affordable antibacterial materials can be developed for potential applications in chronic wound healing device area.

The development of affordable wound care dressings based on biopolymers by employing cost-effective and environmentally safe materials and techniques of fabrication gained an extensive attention from the scientific community^{1–5}. Widely available, inexpensive, biocompatible, biodegradable, non-toxic and renewable, the biopolymers are structural components of the tissues of living organisms and in some cases exhibit biochemical properties that facilitate the wound healing processes^{1,2,5–7}.

A natural polymer and an abundant industrial and domestic waste, the eggshell membrane (ESM) is currently regarded as an interesting platform for designing functionalized architectures with potential applications in water purification⁸, actuators⁹, photocatalysis¹⁰, wound healing products area^{11–20}, etc., some progress being made for its industrial valorization^{21–23}. ESM presents a unique interlaced fibrous 3D network structure formed by fibers with 80–85% proteins in their composition, of which 10% are collagens (types I, V and X) and 70–75% are other proteins and glycoproteins (hyaluronic acid, glucosamine)²⁴. Additionally, ESM possesses a set of essential intrinsic characteristics such as flexibility, high water retention capacity, large surface area and high porosity which favors the diffusion of gas and water molecules and enable the attachment and proliferation of the cells. Due to these features, ESM is capable of mimicking the physico-chemical and biological characteristics of the extracellular matrix and performs similar key functions during wound healing of skin injuries. Hence,

¹National Institute of Materials Physics, Atomistilor 405A, 077125 Magurele, Romania. ²Microbiology Immunology Department, Faculty of Biology, University of Bucharest, Aleea Portocalelor 1-3, 060101 Bucharest, Romania. ³University of Agronomic Sciences and Veterinary Medicine of Bucharest, 011464 Bucharest, Romania. ⁴These authors contributed equally: Nicoleta Preda, Andreea Costas and Mihaela Beregoi. ✉email: nicol@infim.ro; encu@infim.ro

ESM can provide a biological stimulus in this process, being a low-cost alternative to currently wound care products employed for mitigating bacterial infection and for accelerating the wound healing. Furthermore, the functionalization of ESM with inorganic compounds (metals, metal oxides or metal-decorated metal oxides) with already demonstrated antibacterial effect provides a solution to the need for a wound dressing with enhanced functionality. An ideal wound dressing should have simultaneously a good biocompatibility and an adequate antibacterial activity, protecting the injured area from infection and providing a favorable environment (moisture, oxygen and water vapor permeability) for tissue regeneration. However, as far as we know, only three research papers report on the decoration of ESM with inorganic structures with already known antibacterial properties: Ag^{18,19} and Ag-ZnO¹⁷. It is acknowledged that silver prevents bacterial infections in wounds^{25,26}, but for both cost and efficiency related reasons, nanocomposites based on Ag and metal oxides like Ag-ZnO²⁷, Ag-CuO²⁷, Ag and CuO impregnated on Fe doped ZnO²⁸, Cu₂O and Ag co-modified ZnO²⁹, etc. have been recently synthesized by various wet chemical methods. Some metal oxides such as ZnO and CuO exhibit also a pronounced antibacterial activity either as single components³⁰ or as nanocomposites^{31–33}. The two metal oxides present a high potential for application in the field of antibacterial products considering characteristics which include low-price, minimal environmental impact, morphologically rich families of nanostructures which can be relatively easily synthesized by various approaches^{34–37}. Moreover, ZnO is a n-type metal oxide characterized by a wide band gap (~3.37 eV)³⁶, while CuO is a p-type metal oxide with a narrow band gap (generally in the range of 1.2 to 2.16 eV)³⁷. By joining them, a p–n junction can be obtained, a structure which, separates into components the charge carrier pairs produced by visible light irradiation. Further, this process can enhance the generation of highly reactive oxygen species (ROS), these being key mediators of the material's bactericide effect. Additionally, the formation of a p–n junction between ZnO and other semiconductors is an interesting strategy to improve the ZnO stability and its photocatalytic activity, being known that the environmental factors such as solution pH, dissolved oxygen level, particle morphology and UV irradiation can have a significant effect on the ZnO stability during catalysis process³⁸. Accordingly, recent papers focused on the visible-light photocatalytic activity of various p–n heterojunctions based on ZnO such as ZnO/CuO^{39,40}, Bi₂S₃/ZnO⁴¹, ZnO/ZnBi₂O₄⁴² or ZnO/CuBi₂O₄⁴³ shown that such compounds are featured by a good stability maintaining their photocatalytic ability. Moreover, some reports regarding the photocatalytic activity of ZnO deposited by radio frequency (RF) magnetron sputtering put in evidence that the obtained ZnO nanostructured layers are stable even under UV irradiation and can be used as reusable photo-catalysts in aqueous reactions under a wide range of pH medium for photocatalytic applications^{44,45}.

Lately, various physical deposition methods and chemical synthesis were used for designing and developing new architectures based on organic and inorganic compounds for applications in solar cells, photocatalysis, antimicrobial agent domain, optoelectronic devices, biomedical field, etc.^{46–48}. A versatile, high-yield and low-temperature physical vapor deposition technique, magnetron sputtering was employed for preparing thin films on a wide range of substrates. The films are usually polycrystalline, uniform and present good adhesion to the surface of the substrates. Therefore, sputter coating with metal or metal oxide layers can add or enhance antibacterial properties to the biopolymer fibers' surface⁴⁹ or to the non-woven fabrics' surface⁵⁰. Consequently, by sputter coating one can improve the functionality of wound dressing materials. In contrast to the decoration of ESM with inorganic nanostructures through wet chemical methods, the coating and/or decoration by RF magnetron sputtering can result in an inorganic layer with both improved quality and function.

In this context, the present study is focused on the functionalization of eggshell membranes (ESMs) with inorganic materials (Ag, ZnO, CuO used either separately or combined) by using RF magnetron sputtering, a straightforward and scalable deposition technique. In a first step, the ESMs were coated with either Ag, ZnO or CuO layer. Further, the metal oxide-coated ESMs were decorated with Ag nanoparticles for achieving a synergistic antibacterial effect. ESMs covered with metal oxides layers, namely ZnO-coated ESM and CuO-coated ESM were decorated with CuO and ZnO nanoparticles, respectively, in order to form a type of junction which was expected to enhance the antibacterial activity. The morphological, structural, compositional, surface chemistry, optical, cytotoxicity and antibacterial properties of all functionalized ESMs were evaluated and compared to each other. It was found that for the CuO–ZnO based axial p–n junctions, visible light irradiation leads to an enhanced antibacterial activity when tested on *Escherichia coli* (*E. coli*). This antibacterial activity is superior to that observed in the case of ESMs functionalized with silver or with a single type of metal oxide. This is most probably a consequence of charge carrier pairs generated by irradiation and separated in the internal field leading to the development on the surface of ROS which are responsible for bactericide effect.

Experimental section

Preparation of functionalized eggshell membranes. The eggshell membranes (ESMs) were obtained from commercial fresh hen eggs bought from local supermarkets. In the functionalization of ESMs by RF magnetron sputtering, silver (99.99% purity), zinc oxide (99.9% purity) and copper oxide (99.7% purity) sputtering targets with 2 inch in diameter and 0.125 inch in thickness were used, being purchased from Kurt J. Lesker Company Ltd. (UK).

In the first step, ESMs were obtained by manually stripping them from the broken eggshells and washing several times with distilled water. Then, the wet ESMs were mechanically fixed between two overlapping stainless steel frames in order to prevent twisting during the drying process in air at ambient conditions. In the second step, the dried ESMs with dimensions of 2 cm × 3 cm were taken off the supports and functionalized only on one side with metal oxide or/and metal by RF magnetron sputtering (Tetra GmbH Physikalische Instrumente). Hence, for assuring a uniform deposition of the inorganic compounds on the surface of the organic substrates, the ESMs samples were disposed in a circle at an equal distance from the centre of the sample holder (16 cm diameter), this being rotated (4 rot/min) during the deposition process. The vertical distance between the target

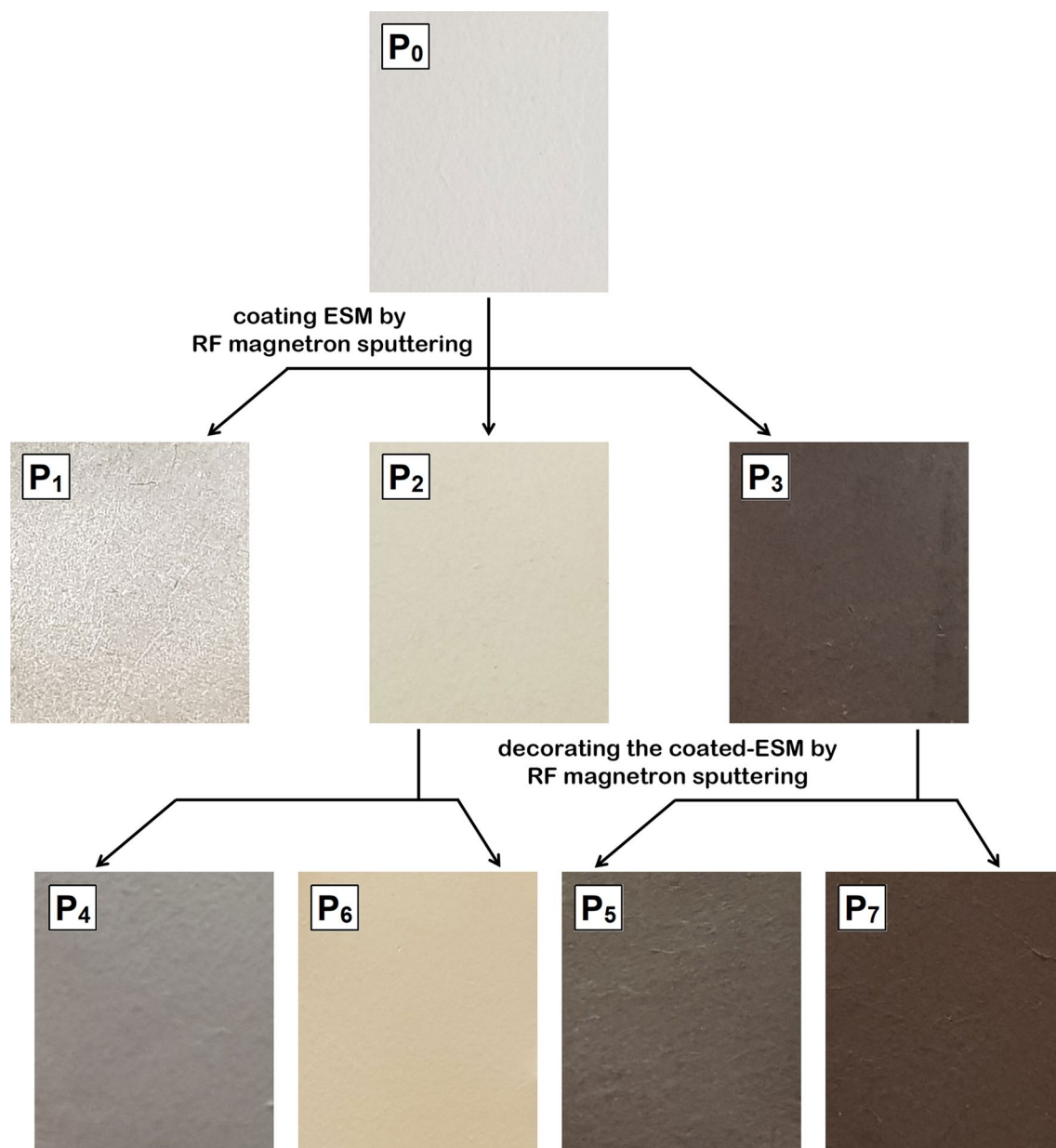


Figure 1. Optical images of native ESM (P_0) and functionalized ESMs (P_1 – P_7).

and the sample holder was 12 cm, the target being pre-sputtered for 20 min, before each deposition, in order to remove any possible contamination from its surface. The deposition process was carried out in an Ar atmosphere with a purity of 9.6 (99.9999%) from Linde. The power applied on the magnetron was 30 W (Ag) or 100 W (ZnO, CuO). During the deposition, the pressure in the chamber was 4.6×10^{-3} mbar (Ag) or 5.4×10^{-3} mbar (ZnO, CuO). For coating the ESMs with a continuous and compact layer, the deposition time was 1 h (Ag) or 3 h (ZnO, CuO). For the decoration with nanoparticles of the layer coated-ESMs, the deposition time was 4 min (Ag) or 6 min (ZnO, CuO).

Images of the investigated samples are presented in Fig. 1, being labeled as follows: P_0 (native ESM), P_1 (Ag-coated ESM), P_2 (ZnO-coated ESM), P_3 (CuO-coated ESM), P_4 (ZnO-coated ESM decorated with Ag nanoparticles), P_5 (CuO-coated ESM decorated with Ag nanoparticles), P_6 (ZnO-coated ESM decorated with CuO nanoparticles) and P_7 (CuO-coated ESM decorated with ZnO nanoparticles).

The visual/color detail is specific for each deposited layer, the white-ivory color of the native ESM being changed in metallic grey (P_1), beige (P_2), brown (P_3), metallic beige (P_5), sand beige (P_6) or dark brown (P_7). Moreover, after functionalization, the surface of ESM is completely and uniformly coated without the appearance of cracks on its surface.

Characterization techniques. A complex characterization of the functionalized ESMs was completed using a set of complementary techniques. The morphology and the elemental composition were analyzed using a

Zeiss Merlin Compact field emission scanning electron microscope (FESEM) and a Zeiss EVO 50XVP scanning electron microscope equipped with an energy dispersive X-ray analysis (EDX) QUANTAX Bruker 200 accessory. At nanoscale level, the morphology, atomic structure and local chemical composition were investigated by high-resolution transmission electron microscopy (HRTEM), EDX including elemental mapping in scanning transmission electron microscopy (STEM) and by selected area electron diffraction (SAED) using a Cs probe-corrected JEM ARM 200F analytical electron microscope.

The crystalline phase was identified by X-ray diffraction (XRD) using a Bruker AXS D8 Advance instrument with Cu K α radiation ($\lambda = 0.154$ nm), the source being operated at 40 kV and 40 mA. The surface chemistry was evaluated by X-Ray photoelectron spectroscopy (XPS) performed in an AXIS Ultra DLD (Kratos Surface Analysis) setup, using Al K α_1 (1486.74 eV) radiation produced by a monochromatized X-Ray source at operating power of 225 W (15 kV \times 15 mA). The base pressure in the analysis chamber was 1.0×10^{-8} mbar. Charge compensation was reached by using a flood gun operating at 1.5 A filament current, 2.7 V charge balance, 1.0 V filament bias. High resolution core level spectra have been recorded using hybrid lens mode, 40 eV pass energy and slot aperture. In the deconvolution of the core level spectra Voigt profiles (singlets or doublets) were used, based on previously described methods⁵¹. The optical properties were investigated by reflectance employing a Perkin-Elmer Lambda 45 UV-VIS spectrophotometer equipped with an integrating sphere. The following software programs were involved in the data acquisition: Zeiss SmartSEM (FESEM), Zeiss SmartSEM and Bruker ESPRIT (SEM/EDX), Olympus Imaging and Image view (HRTEM/STEM/SAED), Bruker DIFFRAC plus BASIC (XRD), Perkin-Elmer UV WINLab (reflectance), Vision (XPS). The analysis of the XPS data was performed using the Igor program, the other experimental data being analyzed by Origin Pro 2017 program.

Biological assessment. The specific properties of the functionalized ESMs were evaluated from cytotoxicity and antibacterial activity perspective. Thus, cytotoxicity was investigated using fluorescent microscopy, MTT assay and oxidative stress assessment. The tests were carried on human mesenchymal amniotic fluid stem (AFS) cells. These are well suited for biocompatibility tests due to their features such as viability, proliferation, protection against the body immune system and differentiation capacity into different types of tissue.

A qualitative evaluation of the AFS cell viability was acquired by fluorescence microscopy (Thermo Fischer Scientific) using the RED CMTPX fluorophore. In DMEM culture medium and in the presence of the investigated sample, the RED CMTPX dye was added at a final concentration of 5 μ M and incubated for 30 min to allow the dye to penetrate the cells. After 5 days, the AFS cells were washed with phosphate buffered saline and visualized, the photomicrographs being taken with an Olympus CKX 41 digital camera driven by CellSense Entry software.

A quantitative evaluation of the AFS cell viability was obtained using a Vybrant MTT Cell Proliferation Assay Kit (Thermo Fischer Scientific). The AFS cells were cultured in DMEM medium supplemented with 10% fetal bovine serum, 1% penicillin and 1% streptomycin antibiotics (all from Sigma-Aldrich). In order to keep the optimal culture conditions, the culture medium was changed twice a week. Hence, the AFS cells were grown, for 72 h, in 96-well plates, with a seeding density of 3000 cells/well in the presence of the investigated samples. Then, 15 ml solution I (2 mM MTT) was added and incubated at 37 $^{\circ}$ C for 4 h. Next, for dissolving the formed formazan crystals, solution II (1 mg sodium dodecyl sulfate in 10 ml 0.01 M HCl) was added by pipetting it vigorously. After 1 h, the absorbance at 570 nm wavelength was recorded using a TECAN Infinite M200 spectrophotometer.

The oxidative stress for AFS cells was analyzed by GSH-Glo Glutathione Assay Kit (Promega). The AFS cells were seeded for 24 h at a density of 3000 cells in 300 μ l of DMEM culture medium supplemented with 10% fetal bovine serum and 1% antibiotics (penicillin, streptomycin/neomycin) in 96-well plates and in the presence of the investigated sample. Afterwards, 100 μ l 1X GSH-Glo Reagent was added and incubated at 37 $^{\circ}$ C for 30 min. Then, 100 μ l Luciferin Detection Reagent was also added and incubated at 37 $^{\circ}$ C for another 15 min. Subsequently, the cells were homogenized and the plate was investigated using a Microplate Luminometer Centro LB 960.

Further, the antibacterial activity was evaluated against non-pathogenic *Escherichia coli* (*E. coli* ATCC 25922) strain, as Gram-negative bacteria model, in both planktonic and biofilm growth state. Thus, for planktonic cells, 2 ml tryptic soy broth (TSB) and 20 μ l microbial suspension with 0.5 McFarland density (1.5×10^8 CFU/mL) were added on the sterilized investigated samples placed in 6-well plates. After 24 h incubation at 37 $^{\circ}$ C, the turbidity of the culture medium was determined by measuring the absorbance at 620 nm with a Biotek Synergy-HTX ELISA multi-mode reader spectrophotometer. In the case of biofilms, after incubation, the investigated samples were washed in sterile saline solution in order to remove the non-adherent bacteria, while the adherent bacteria remained attached to the respective samples. Next, they were introduced into Eppendorf tubes with 1 ml sterile saline and vortexed for 30 s. From the suspension recovered in sterile saline, decimal dilutions were obtained and seeded in triplicate (3 replicates of 10 μ l each) on agar medium in order to calculate the number of CFU (colony forming units)/ml. The antibacterial activity of the functionalized ESMs was also evaluated under exposure to the visible light which was provided by a commercially LED lamp, Vorel 82730 (100 mW power). In this case, the sterilized investigated samples were placed in 6-well plates containing $\sim 10^5$ CFU/ml microbial suspension, the incubation being carried out at 37 $^{\circ}$ C for 3 h, 6 h and 9 h under illumination with the LED lamp. At the end of each incubation time, decimal dilutions obtained from the suspension recovered in sterile saline were seeded in triplicate (3 replicates of 10 μ l each) on agar medium for evaluating the number of colonies. An *E. coli* solution used as a control sample was investigated in the same experimental conditions but in the absence of a functionalized ESM. According with a previous article⁵², the antibacterial efficacy of the investigated samples was calculated in terms of log reduction (LR) and percentage of bacterial cell reduction (R, %) using the following equations:

$$LR = \log_{10}(\text{untreated viable cell density}/\text{treated viable cell density})$$

$R\% = [(CFU_c - CFU_p)/CFU_c] \times 100\%$; where CFU_c and CFU_p represent the numbers of CFU/ml for the control and each investigated sample.

It has to be mentioned that the biological tests were carried out in three replicates. Each replicate was performed in triplicate. The experiments were repeated two times in triplicates. In the biological assays, the statistical data were analyzed using the Origin Pro 7.5 software.

Results and discussions

The morphology of native and functionalized ESMs was analyzed by FESEM, the images being presented at low and high magnification in Figs. 2 and 3, respectively. Thus, the structure of P_0 sample consists in a macroporous network featuring highly cross-linked smooth fibers with diameter sizes in the micrometer range and pores of several micrometers.

The FESEM images of all functionalized ESMs, P_1 – P_7 sample (Fig. 2), indicate that the typical 3D porous network of the ESM is successfully preserved during its functionalization, the deposition parameters employed in the RF magnetron deposition process being adequate chosen for avoiding the embedding of the ESM fibers into a metallic or metal oxide thick layer. A continuous and uniform film of either metal or metal oxide was deposited on the surfaces of the fibers.

The FESEM images at higher magnification of all functionalized ESMs (Fig. 3) reveal that P_1 , P_2 and P_3 samples are coated with nanostructured self-assembled films consisting of nanoparticles having a relatively homogeneous size, ~ 15 nm (Ag) and ~ 20 nm (ZnO and CuO).

The cross-section FESEM images (Fig. 2 insets) emphasize the hybrid structure based on an organic core and an inorganic shell. Also, from these images, the thickness of the inorganic shell was estimated as being ~ 130 nm for P_1 sample, ~ 300 nm for P_2 and P_3 samples and ~ 320 – 330 nm for P_4 – P_7 samples. For improved resolution in the case of the cross-section FESEM imaging, the deposition of a thin layer of gold (~ 20 nm) was necessary.

The elemental distribution on the ESM surface and the composition of the samples were evaluated by EDX spectroscopy, the mapping images and the corresponding spectra being given in Fig. 4. The EDX mapping images illustrate that all functionalized ESMs present a uniform distribution of the chemical elements on their surfaces. The EDX spectrum of P_0 sample reveals the presence of the typical elements, C, N, O and S, which can be found in the ESM structure¹⁸. In addition, a signal corresponding to Au is also observed because, as we already mentioned, a thin layer of gold was sputtered on the surface of the native ESM prior to its morphological investigation. In the EDX spectra of P_1 – P_7 samples, the simultaneously presence of the signals corresponding to the ESM elements with those associated to Ag in P_1 , P_4 and P_5 samples, to Zn in P_2 , P_4 , P_6 and P_7 samples and to Cu in P_3 , P_5 , P_6 and P_7 samples confirms the ESM functionalization. Based on the EDX analysis, the atomic percentage of the elements contained in the functionalized ESMs was evaluated (Table S1). Thus, in the inorganic compact layer, the atomic percentage was estimated at $\sim 18\%$ for Ag and between 32 and 38% for Zn and Cu while in the case of the decorated inorganic nanoparticles, the atomic percentage was evaluated at $\sim 1\%$ for these three elements.

The structural information of the native and functionalized ESMs samples was obtained by XRD analysis (Fig. 5). The XRD pattern of P_0 sample indicates the amorphous character of ESM related to its composition based on amine, amides and carboxylic compounds.

The peaks at 2θ : 38.2° , 44.4° , 64.6° and 77.5° observed in the XRD pattern of P_1 sample are indexed to (111), (200), (220) and (311) planes of the face-centered cubic Ag structure (JCPDS 04–0783). The XRD patterns of P_2 sample exhibit peaks at 2θ : 31.9° , 34.2° , 36.3° , 47.3° , 56.7° , 62.6° and 68.0° associated to (100), (002), (101), (102), (110), (103) and (112) planes of the hexagonal wurtzite ZnO structure (ICDD 00-035-1451). The XRD pattern of P_3 sample displays peaks at 2θ : 35.2° and 38.7° corresponding to (110) and (11–1) planes of the monoclinic CuO structure (ICDD 00-048-1548).

In the XRD patterns of P_4 and P_5 samples, the presence of peaks at $\sim 38.5^\circ$ (P_4) and $\sim 44.3^\circ$ (P_5) prove the existence of the Ag nanoparticles on the ZnO layer (P_4) and CuO layer (P_5), respectively. However, in the XRD patterns of P_6 and P_7 samples, the diffraction signature of the metal oxide nanoparticles employed for the decoration had not been detected, only the characteristic diffraction peaks assigned to the metal oxide which form the compact layer deposited on the surface of ESM, hexagonal wurtzite ZnO (P_6) and monoclinic CuO (P_7), respectively being clearly identified.

Therefore, in order to certify the chemical composition of the inorganic shell and the oxidation states of each constituent, all samples were investigated by XPS, their spectra being presented in Fig. 6. The peaks observed in the XPS spectra of Ag 3d, Zn 2p and Cu 2p were indexed as follows: (i) the peaks at ~ 368 eV and ~ 374 eV to Ag $3d_{5/2}$ and Ag $3d_{3/2}$ levels of Ag (0)^{53,54}; (ii) the peaks at ~ 1021 eV and ~ 1045 eV to Zn $2p_{3/2}$ and Zn $2p_{1/2}$ levels of Zn²⁺ in ZnO^{40,55} and (iii) the peaks at ~ 933 eV and ~ 954 eV to Cu $2p_{3/2}$ and Cu $2p_{1/2}$ levels of Cu²⁺ in CuO^{40,55}. For native ESM, the broad peak at ~ 531.5 eV from the XPS spectra of O 1s represents the different oxygen environments in the protein amino acids^{56,57} while the peaks at ~ 284.5 eV, ~ 285.5 eV and ~ 287.5 eV from the XPS spectra of C 1s can be correlated to C–C, C–N and C=O bonds, respectively^{56,57}. In the XPS spectra of O 1s for functionalized ESMs, the broad peak at ~ 529 – 530 eV can be attributed to O²⁻ state in metal oxides (ZnO and CuO)^{40,55}. It can be noticed the shift of this peak to ~ 531 eV, responsible for this shift being, most probably, a contamination of the surfaces with carbonate from the environment. Moreover, the deconvolution obtained by Voigt profiles of the core level spectra of Ag 3d (Figure S1), Zn 2p (Figure S2) and Cu 2p (Figure S3) were also analyzed for evidencing the presence of other species of these inorganic elements. Thus, the deconvolution of the XPS spectra for the core level Ag $3d_{5/2}$ shows a broad peak with two components confirming the hypothesis concerning the existence of more than one silver species. The signal centered at 368.0 eV (P_1) or 368.2 eV (P_4 and P_5) confirms the existence of free metallic silver atoms (Ag (0)), in agreement with reported data for Ag foil⁵³ and Ag nanoparticles⁵⁴. Meanwhile, the signal centered at 369.0 eV (P_1), 368.9 eV (P_4) or 368.8 eV (P_5) can indicate positively charged silver atoms (Ag (0) + δ), these resulting, as it is suggested in the literature, from the slight oxidation in air of the metallic atoms situated on the surface of the silver layer and exposed to ambient conditions^{58,59} or from the silver interaction with a relatively high electronegative atom (oxygen, nitrogen

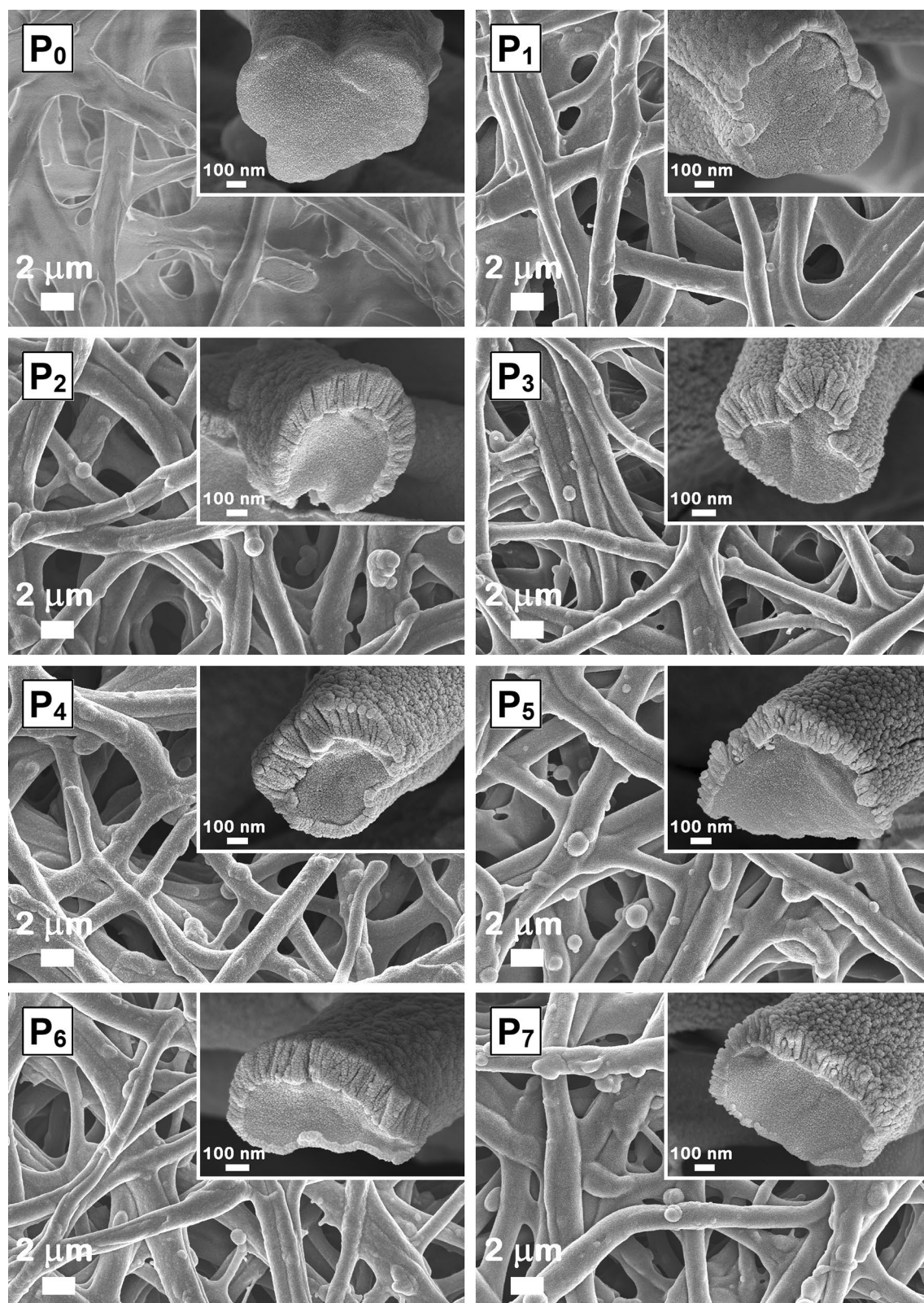


Figure 2. FESEM images of native ESM (P_0) and functionalized ESMs (P_1 – P_7). Insets: cross-sectional FESEM images of the corresponding samples.

or sulphur)^{56,60,61}. It is also worth noticing that comparatively with the binding energy indexed to the metallic silver, the oxidized Ag-bulk is characterized by lower binding energy while, in striking contrast, the air-exposed

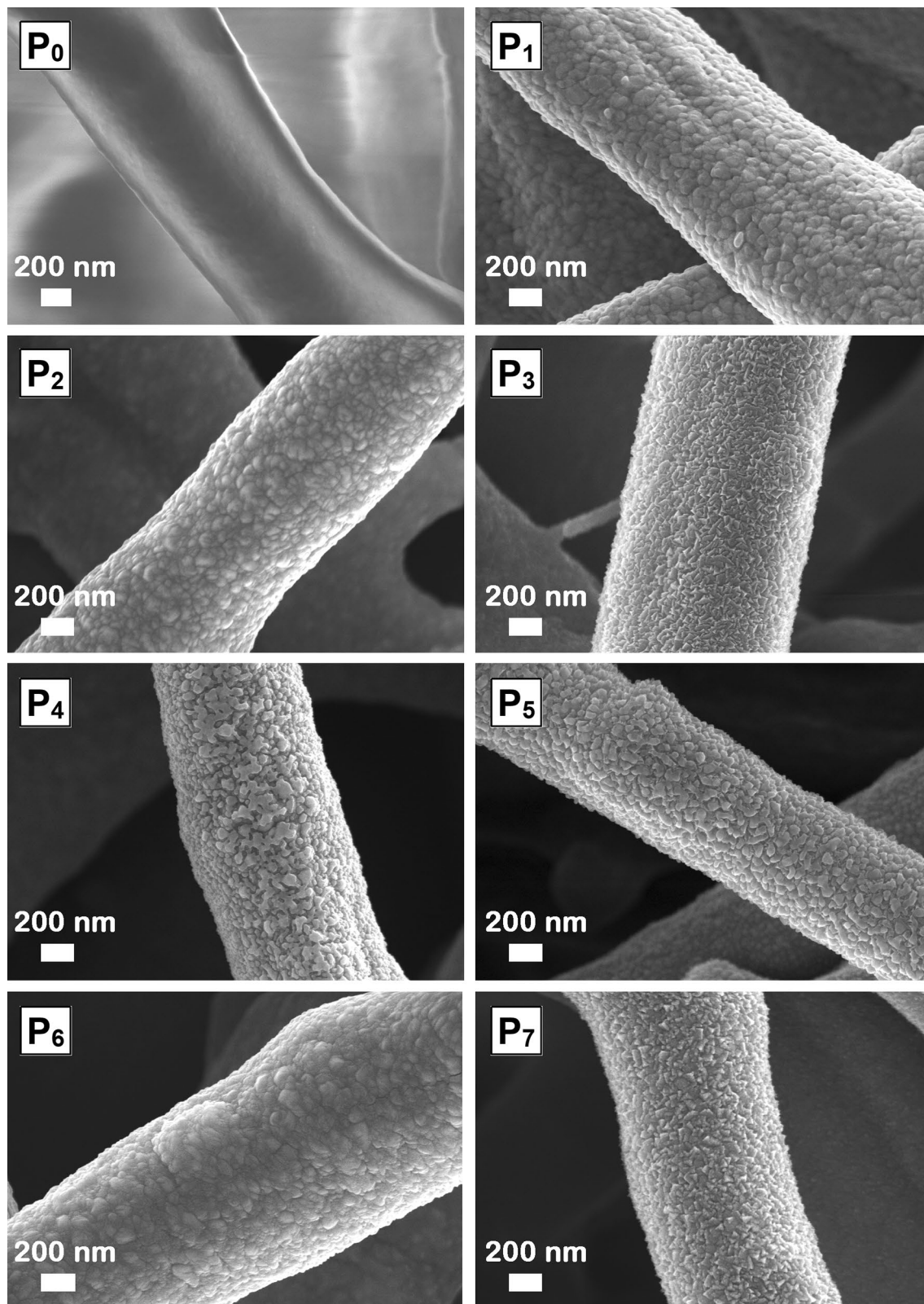


Figure 3. FESEM images at higher magnification of native ESM (P_0) and functionalized ESMs (P_1 – P_7).

Ag nanoparticles exhibit higher binding energy⁶². The deconvolution of the XPS spectra for the core level Zn $2p_{3/2}$ reveals a narrow peak centred at 1020.9 eV (P_2), 1021.9 eV (P_4), 1021.1 eV (P_6) or 1021.2 eV (P_7) assigned to Zn^{2+} state in ZnO, consistent with the previously reported data^{40,55}. The deconvolution of the XPS spectra for

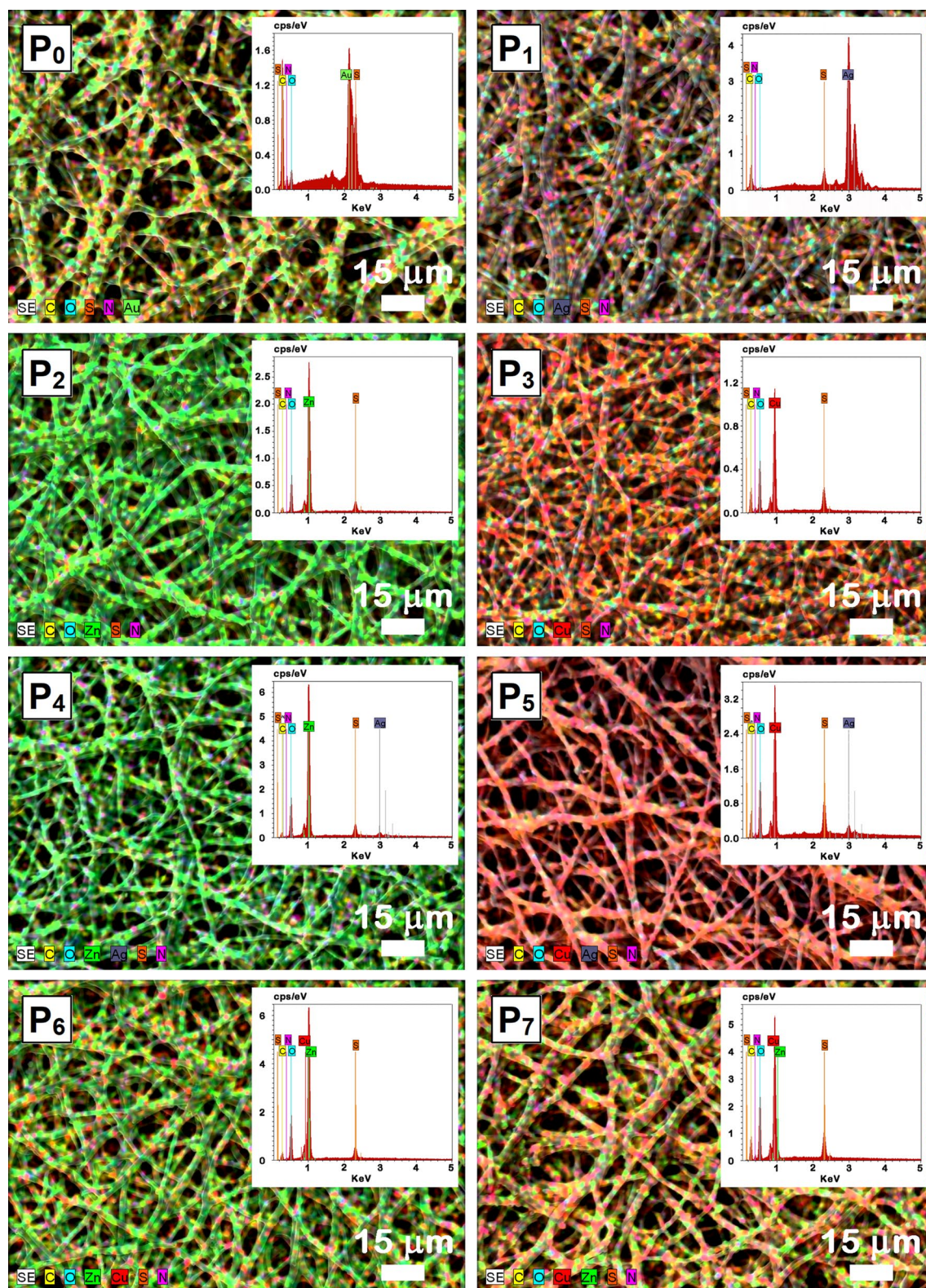


Figure 4. EDX mapping images of native ESM (P₀) and functionalized ESMs (P₁–P₇). Insets: EDX spectra of the corresponding samples.

the core level Cu 2p_{3/2} exhibits a broad peak with two components, one centered at 933.1 eV (P₃), 932.9 eV (P₅), 933.0 eV (P₆) or 932.6 eV (P₇) associated with Cu²⁺ state in CuO, in accordance with reported data^{40,55} and other at 934.9 eV (P₃), 934.8 eV (P₅), 934.8 eV (P₆) or 934.5 eV (P₇) linked most probably to a slight contamination of

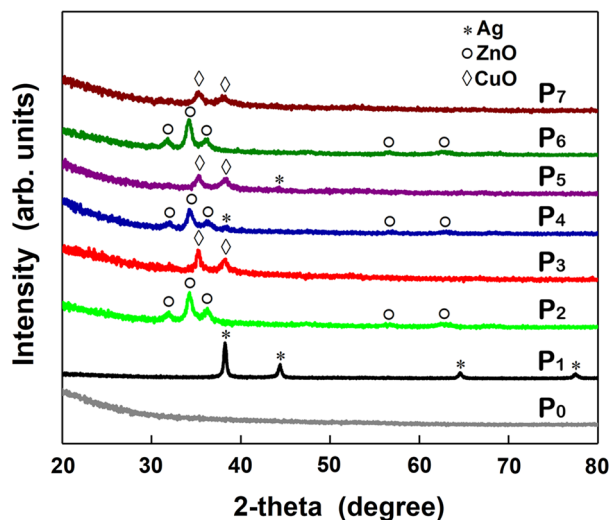


Figure 5. XRD patterns of native ESM (P_0) and functionalized ESMs (P_1 – P_7).

the surfaces with carbonate from the environment. Additionally, the formation of CuO is demonstrated by the presence of the satellite peaks at ~ 940 – 945 eV and ~ 964 eV characteristic only to the bivalent oxidation state of Cu^{40,55}. Consequently, the XRD data and the XPS results confirm the presence of Ag in P_1 , P_4 and P_5 samples, ZnO in P_2 , P_4 , P_6 and P_7 samples and CuO in P_3 , P_5 , P_6 and P_7 samples.

The optical properties of the native and functionalized ESMs were analyzed by diffuse reflectance (Fig. 7). In the case of P_0 sample, the reflectance spectrum displays a decrease at ~ 330 nm, in accordance with that reported in the literature for the native ESM^{63,64}. A weak decrease at ~ 405 nm is barely noticed in the reflectance spectrum of P_1 sample owed to a weak surface plasmon resonance (SPR) effect induced by the Ag film deposited on the surface of the ESM⁶⁵. In the reflectance spectra of P_2 and P_3 samples, a strong decrease can be observed below ~ 420 nm (P_2) and ~ 860 nm (P_3) due to the band-to-band transition in ZnO and CuO, respectively, in agreement with those previously reported^{36,37}.

The reflectance spectra of P_4 – P_7 samples are dominated by the optical signature of the metal oxide layer deposited on the ESM surface, ZnO (P_4 and P_6) or CuO (P_5 and P_7). However, in the case of P_4 , additionally to the strong decrease peak related to the ZnO, two characteristic plasmon bands are clearly identified at ~ 435 nm and ~ 590 nm, similar with those observed in other studies^{66,67}. The result can be explained taking into account that in this case the Ag nanoparticles decorate the surface of the metal oxide-coated ESM in comparison with P_1 where the Ag nanoparticles formed a compact and uniform film on the surface of the ESM. It is noteworthy that the presence, position and intensity of the SPR band associated to the Ag nanoparticles is strongly influenced by many parameters of the nanoparticles such as size, shape, inter-particle distance, surface chemistry, surrounding environment, etc⁶⁸.

Using the reflectance data and Kubelka–Munk function, where $F(R) = (1 - R)^2/2R$ and R was the observed diffuse reflectance, the band gap value of ZnO was evaluated at approximately 3.1 ± 0.1 eV while the band gap of CuO was estimated at approximately 1.6 ± 0.2 eV.

Further, in order to evidence the formation of the p–n junction between the ZnO and CuO, both functionalized ESMs containing a combination of the two metal oxides, meaning ZnO-coated ESM decorated with CuO nanoparticles (P_6 sample) and CuO-coated ESM decorated with ZnO nanoparticles (P_7 sample) were investigated by various TEM techniques, the obtained data being shown in Fig. 8. The samples for the TEM measurements were prepared by crushing the functionalized ESM in a mortar and dispersed in ethanol, a droplet of this suspension being deposited on TEM grids. Thus, the STEM images and the EDX elemental mappings of P_6 and P_7 samples put in evidence the formation of the CuO–ZnO p–n junction by the presence of Cu K and Zn K elements. It can be observed the spatial distribution of these two elements in the p–n junction: in P_6 sample, Zn K is presented in the inner part and Cu K in the outer part while in P_7 sample, Cu K is presented in the inner part and Zn K in the outer part. These results confirm the formation of p–n junction in two configurations in accordance with the metal oxide deposition sequences involved in the preparation of P_6 and P_7 samples. Moreover, the thickness of the outer layer (Cu K for P_6 and Zn K for P_7) was estimated at ~ 20 – 30 nm, in agreement with the cross-section FESEM images (Fig. 2). The HRTEM image acquired on P_7 sample revealed that the CuO–ZnO p–n junction is formed by ZnO and CuO crystallites, the corresponding SAED pattern exhibiting the crystalline hexagonal wurtzite structure of the ZnO outer layer in agreement to the XRD data (Fig. 5).

The biocompatibility of the native and functionalized ESMs was evaluated in relation to human mesenchymal AFS cells by applying standard protocols for fluorescence microscopy, MTT assay and GSH assay.

The fluorescent images from Fig. 9 evidence that the mesenchymal AFS cells cultured on the investigated samples have similar morphological features with the control sample (Figure S4). After 5 days in the presence of the functionalized ESMs, the cells incorporating the fluorescent CMTPIX dye into the cytoplasm prove that the

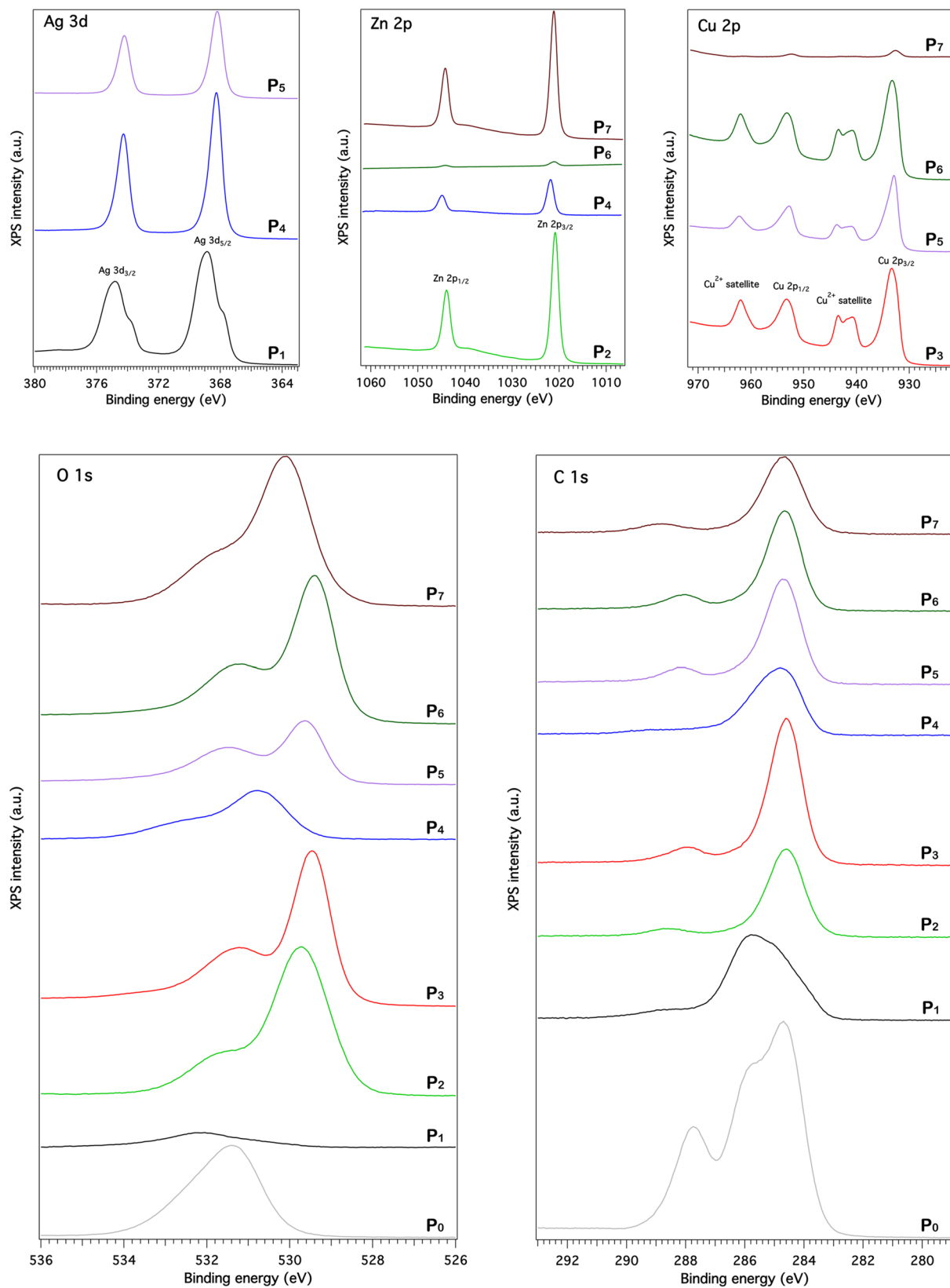


Figure 6. XPS spectra for the Ag 3d, Zn 2p, Cu 2p, O 1s and C 1s core levels in native ESM (P₀) and functionalized ESMs (P₁-P₇). Artificial intensity offsets are introduced for clarity.

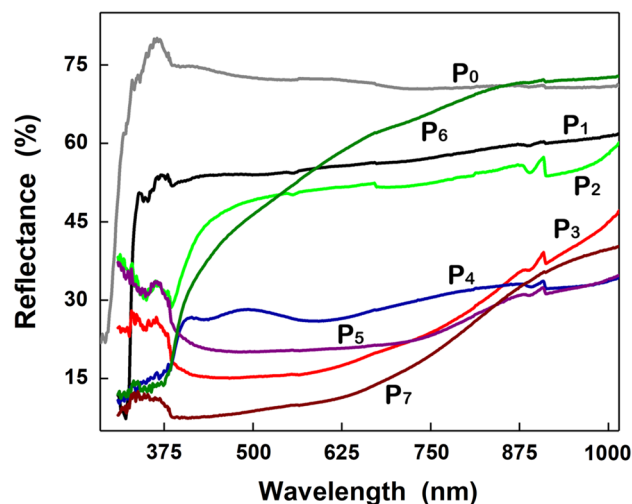


Figure 7. Reflectance spectra of native ESM (P_0) and functionalized ESMs (P_1 – P_7).

cells are viable, with an active metabolism. Also, the fluorescent images of the analyzed area reveal the adhesion and homogeneous distribution of the mesenchymal AFS cells on the surface of the investigated samples.

Further, the cell viability and proliferation of the investigated samples were tracked by the MTT assay and the oxidative stress caused by these materials by GSH assay, the results being displayed in Fig. 10 left and Fig. 10 right, respectively. In the MTT assay, the recorded intensity for absorbance at 570 nm is proportional to the enzymatic activity of the cells consequently with their viability. In this context, the MTT tests confirmed that after 72 h of incubation, the mesenchymal AFS cells have a normal metabolism and growth in the presence of all functionalized ESM since only a smaller decrease, within the limit of 9% of the absorbance values, is noted in comparison with that related to the control sample. In the GSH assay, the amount of a natural antioxidant, glutathione, produced by cells during a normal functioning process was estimated, a high value recorded for this parameter indicating pathological changes in the cells. In our case, the GSH tests indicate that after 24 h of incubation, the presence of any functionalized ESM does not induces significant oxidative stress in the mesenchymal AFS cells, the GSH level being slightly higher within the limit of 14% as compared with that associated to the control sample. In both cases, MTT and GSH assays, the low difference between the recorded data and those obtained for the control sample are not of significant biological value. Consequently, the functionalized ESMs are well accepted by the mesenchymal AFS cells with no significant cytotoxic effect, the result emphasizing the potential of using them as biocompatible materials.

The antibacterial activity of native and functionalized ESM was investigated against *E. coli* in planktonic and biofilm states, the recorded values being presented in Fig. 11 left and Fig. 11 right, respectively.

E. coli was used in both states for comparing the interaction of the samples either with solitary planktonic cells or with biofilm bacteria, the latter being in fact an irregularly structured community of cells with a surface encased in an extracellular polymeric matrix⁶⁹. Based on the data provided by both figures and without taking into account the native ESM, the following series regarding the antibacterial response of the functionalized ESMs are obtained: $P_1 > P_5 > P_3 > P_6 > P_4 > P_2 > P_7$ in the case of *E. coli* planktonic state and $P_5 > P_3 > P_6 > P_7 > P_4 > P_2 > P_1$ in the case of *E. coli* biofilm state. It has to be emphasized the particular behavior of Ag-coated ESM (P_1), meaning that *E. coli* biofilms are more resistant to silver inhibition than *E. coli* planktonic cells. The result is consistent with previous data reported on the interactions of nanosilver with *E. coli*⁷⁰. Nevertheless, CuO-coated ESM decorated with Ag nanoparticles (P_5) and CuO-coated ESM (P_3) are the two samples that present a good antibacterial activity in the case of both *E. coli* states. The antibacterial response of these samples can be assessed based on the charge carriers produced by this semiconductor.

In order to improve the antibacterial activity of the ESM functionalized with metal oxides (P_2 , P_3 , P_6 and P_7 samples) through the activation of a p–n junction under illumination, these samples were exposed 3, 6 and 9 h to the visible light given by a commercially LED lamp, the result being shown in Table 1. Hence, on 9 h exposure, the reduction in bacterial growth increases from ~40% to ~54% for ZnO-coated ESM (P_2) and from ~33% to ~52% for CuO-coated ESM (P_3). Meanwhile, on 9 h exposure, the reduction in bacterial growth increases from ~5% to ~45% for ZnO-coated ESM decorated with CuO nanoparticles (P_6) and from ~27% to ~82% for CuO-coated ESM decorated with ZnO nanoparticles (P_7).

According with the schematically representation from Fig. 12, the strongest bactericide effect observed in the last mentioned sample can be explained based on its particular architecture consisting in a compact inner absorbing layer (CuO, a semiconductor with a narrower bandgap) and a non-continuous outer window layer formed by nanoparticles (ZnO, a semiconductor with a wider band gap). The configuration of this axial p–n junction favours a high absorption of the visible light in the uncovered regions on the CuO compact layer and an efficient charge separation process induced by type II band alignment (staggered gap) formed at the interface between the two metal oxides^{40,71}. Further, the generated charge carriers in the semiconductor materials can

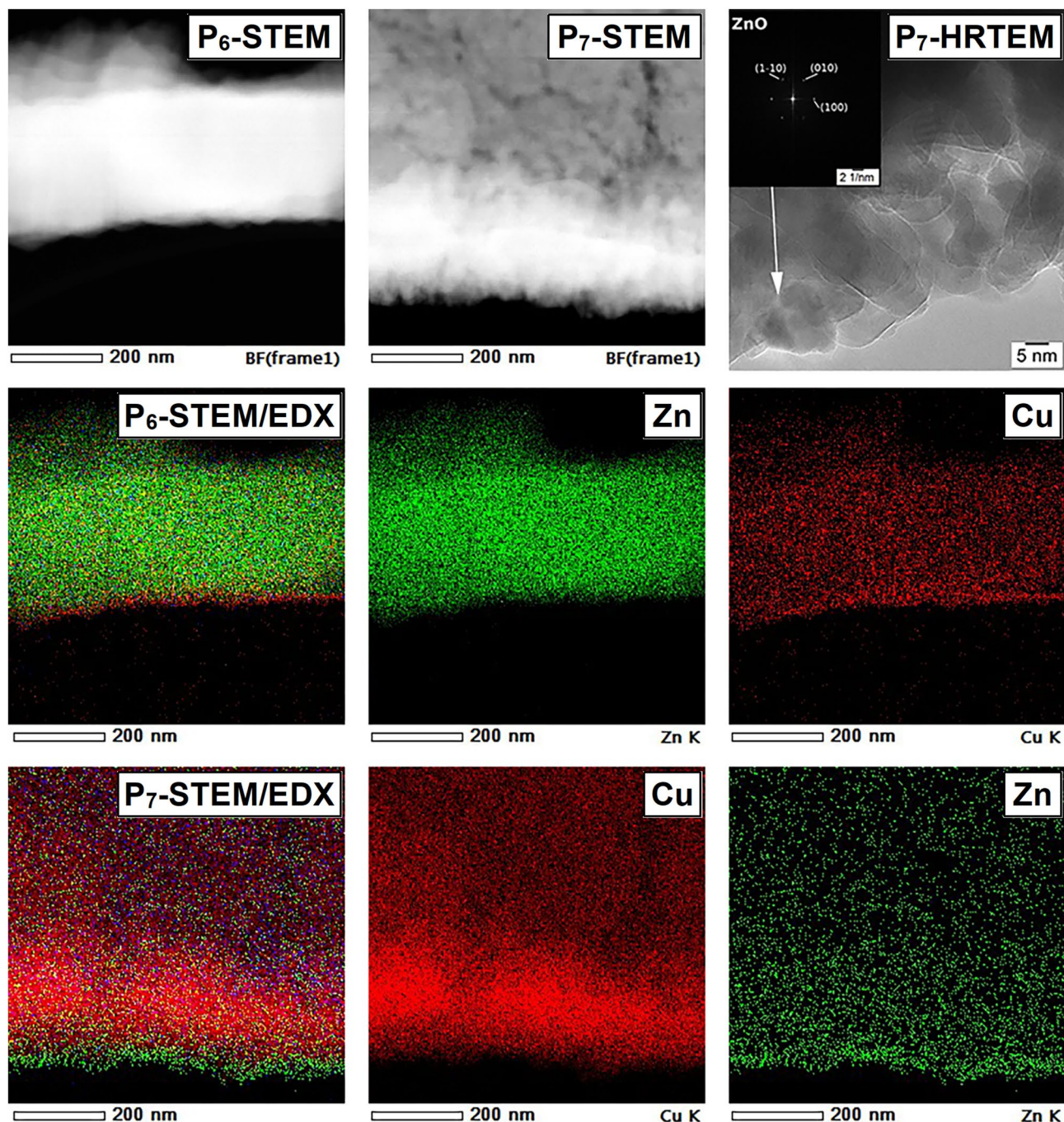


Figure 8. STEM images and EDX elemental mappings including the spatial distribution of the Zn and Cu elements in the functionalized ESMs (P_6 and P_7), HRTEM image and SAED pattern exhibiting the ZnO crystalline structure (inset) in P_7 sample.

promotes the formation on their surface of ROS species, these being toxic to bacteria (by various mechanisms leading to the cell membrane rupture)^{72,73}.

An important aspect regarding the stability of the CuO-ZnO p-n junction must be emphasized: no significant photo-corrosion effect was observed after the illumination with the LED lamp. The FESEM images and EDX data (Figure S5) obtained on the CuO-coated ESM decorated with ZnO nanoparticles (P_7 sample) after visible light irradiation shown that the inorganic nanoparticles kept their shape and the fact that the Zn is presented almost in the same atomic percentage with that evaluated in the same sample before illumination.

Additionally, the change induces in the *E. coli* morphology by the antibacterial activity of the p-n junction under visible light can be observed in the FESEM images of this bacteria on the native ESM (P_0 sample) and on the CuO-coated ESM decorated with ZnO nanoparticles (P_7 sample). Thus, on P_0 sample, the healthy *E. coli*

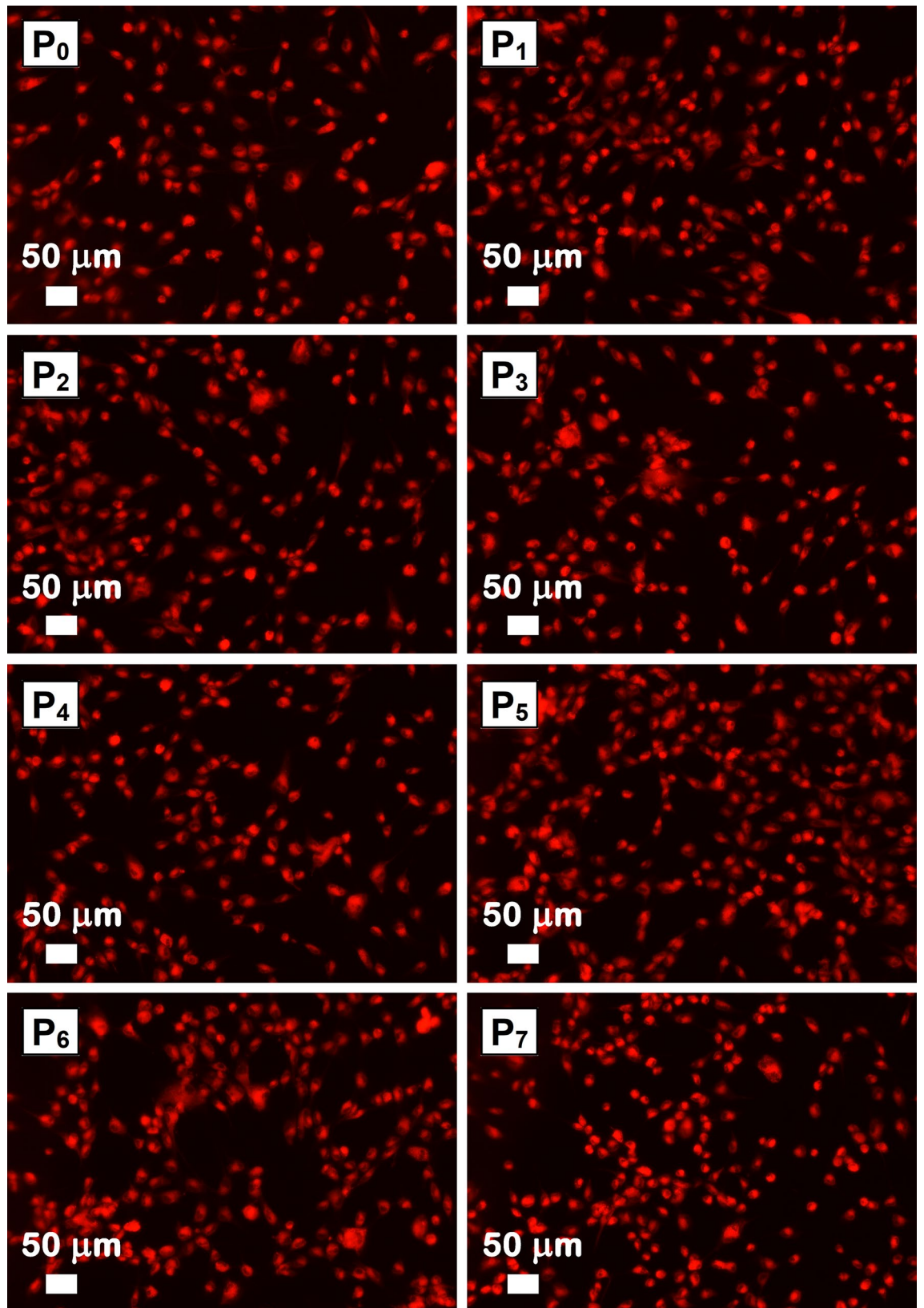


Figure 9. Fluorescence microscopy images of cells cultured on the native ESM (P₀) and functionalized ESMs (P₁–P₇).

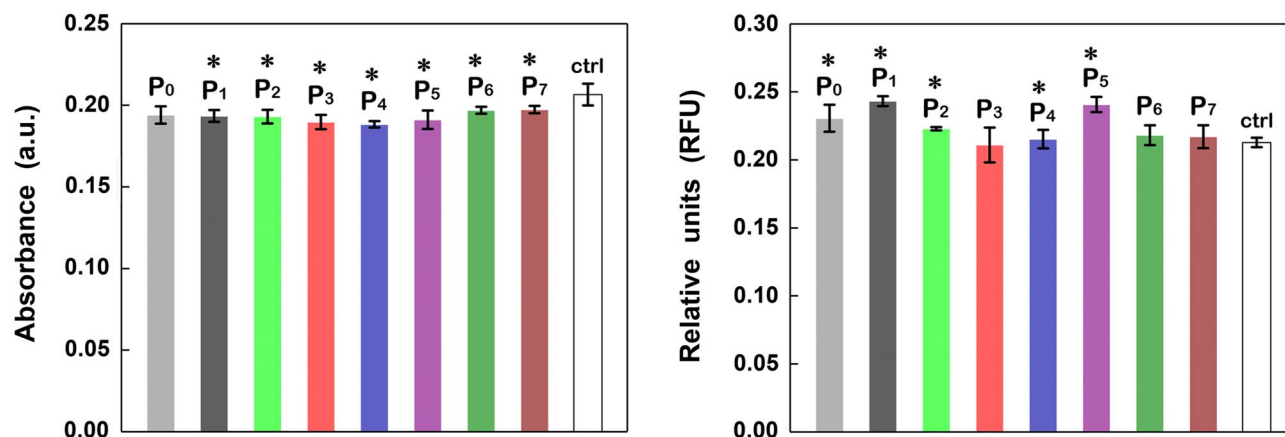


Figure 10. MTT (left) and GSH (right) analysis of the native ESM (P_0) and functionalized ESMs (P_1 – P_7). Statistical significance was assessed using two-tailed Student's t-test; the results are represented as mean \pm standard error, * $P < 0.05$ compared to control, $n = 3$.

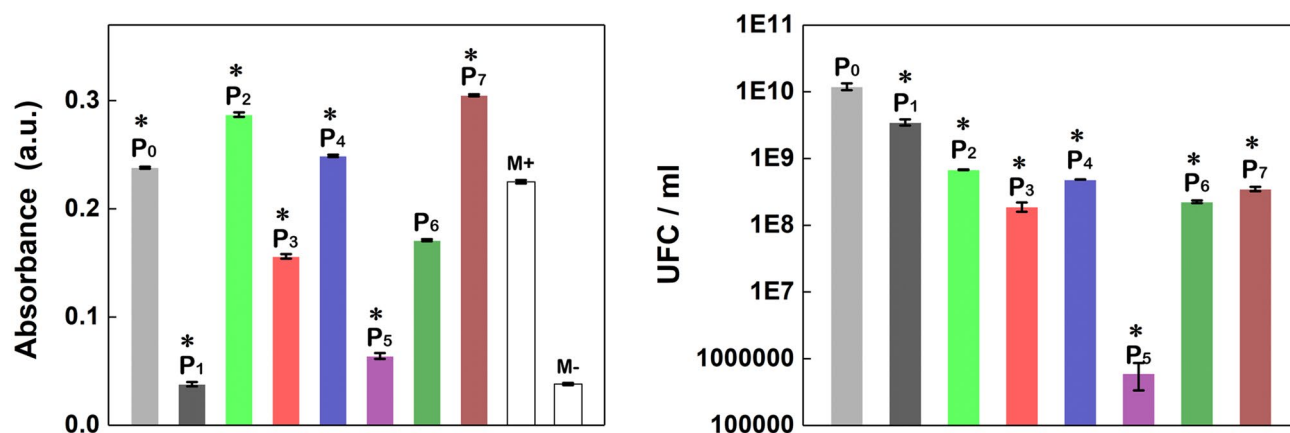


Figure 11. *E. coli* planktonic cells (left) and *E. coli* biofilm (right) inhibition growth analysis of the native ESM (P_0) and functionalized ESMs (P_1 – P_7). Statistical significance was assessed using two-tailed Student's t-test; the results are represented as mean \pm standard error, * $P < 0.05$ compared to control M+ / M- = bacterial suspension/ bacterial growth media, $n = 3$.

Sample exposed to visible light	3 h			6 h			9 h		
	CFU ml ⁻¹	LR	R %	CFU ml ⁻¹	LR	R %	CFU ml ⁻¹	LR	R %
P_2	2×10^5	0.224	40.24	1×10^5	0.279	47.37	4×10^5	0.336	53.85
P_3	2×10^5	0.173	32.93	1×10^5	0.200	36.84	5×10^5	0.323	52.45
P_6	3×10^5	0.022	4.878	0.9×10^5	0.309	50.88	5×10^5	0.258	44.76
P_7	2×10^5	0.136	26.83	0.5×10^5	0.525	70.18	2×10^5	0.740	81.82

Table 1. Antibacterial efficiency of functionalized ESMs (P_2 , P_3 , P_6 and P_7) against *E. coli* under exposure to visible light.

is featured by its characteristic shape, a rod with spherical caps, with a smooth and intact surface, while on P_7 sample, the dead *E. coli* revealed an irregular shape due to the membrane collapse.

The outcome of the experiments confirms that an efficient bactericidal effect can be achieved, under visible light irradiation, in the case of the ESM functionalized with low cost and abundant metal oxides (ZnO, CuO) by employing a cost effective and scalable deposition technique (RF magnetron sputtering).

Conclusions

Eggshell membranes (ESMs) were functionalized with inorganic materials (individual or a combination of Ag, ZnO, CuO) by RF magnetron sputtering, a straightforward deposition technique. The ESM was first coated with a Ag, ZnO or CuO continuous layer, further the metal oxide-coated ESMs being decorated with Ag nanoparticles

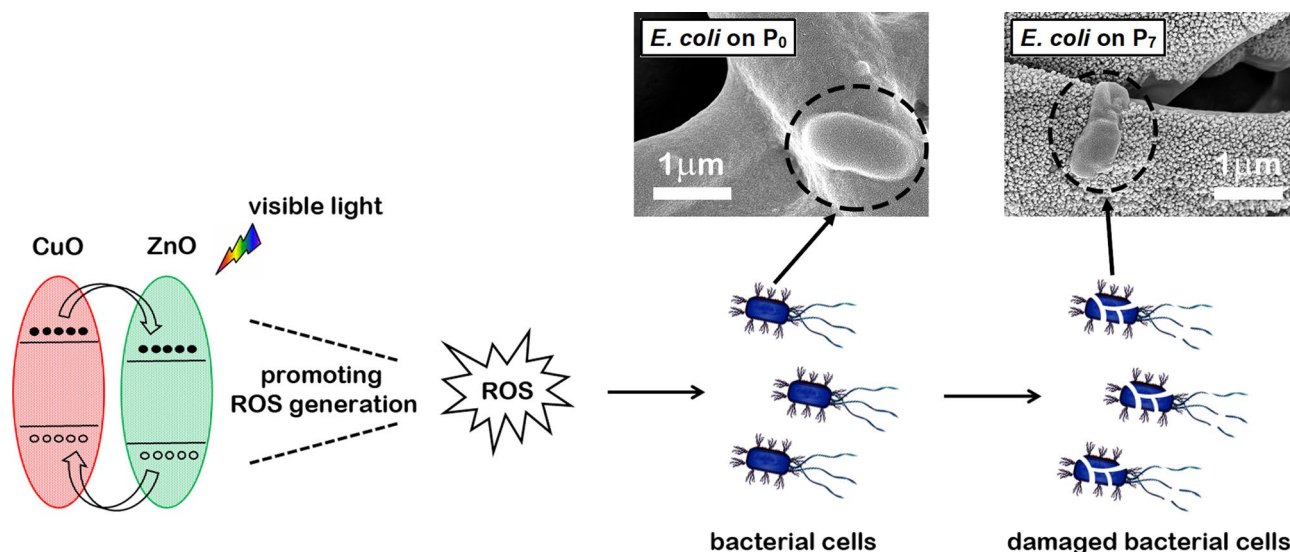


Figure 12. Schematic representation of the enhancement of antibacterial performance under visible light in the CuO-ZnO p-n junction. The FESEM images of an *E. coli* on the native ESM (P₀) and on the functionalized ESM (P₇).

while other ZnO-coated ESM and CuO-coated ESM being decorated with CuO and ZnO nanoparticles, respectively. The typical 3D porous network of the ESM is successfully preserved during its functionalization, the surface of the organic fibers being coated with a continuous and uniform inorganic film. Physico-chemical characterization of the functionalized ESMs confirms the presence of the inorganic components (Ag, ZnO and CuO) on the ESM surface. The cytotoxicity of functionalized ESMs was evaluated by fluorescence microscopy, MTT assay and GSH assay, the recorded data evidencing their biocompatibility potential, the materials being well accepted by the mesenchymal AFS cells with no significant cytotoxic effect. Further, the antibacterial activity of functionalized ESMs was analyzed against *E. coli* in planktonic and biofilm states. A particular behavior was observed in the case of Ag-coated ESM (P₁), *E. coli* biofilms being more resistant to silver inhibition than *E. coli* planktonic cells. From all functionalized ESMs, CuO-coated ESM decorated with Ag nanoparticles (P₂) and CuO-coated ESM (P₃) are the two samples that present a good antibacterial activity in the case of both *E. coli* states. Under exposure to visible light from a commercially LED lamp, the CuO-coated ESM decorated with ZnO nanoparticles (P₇) exhibits improved antibacterial performance due to the formation of an axial p-n junction between the two metal oxides which enhances the generation of highly reactive oxygen species favoring the bacteria killing. The outcome of this study proves that by tailoring specific properties, materials with enhanced antibacterial properties under visible light can be fabricated. Using a cost-effective and environmentally safe path which involves an abundant industrial bio-waste (ESM), low-cost metal oxides (ZnO and CuO) and a straightforward deposition technique (RF magnetron sputtering) is an added benefit. Such materials can be excellently suited as a component for affordable wound dressing with intense antibacterial activity.

Data availability

The datasets supporting the conclusions of the current study are presented in the manuscript and supporting information.

Received: 28 August 2020; Accepted: 17 November 2020

Published online: 01 December 2020

References

1. Suarato, G., Bertorelli, R. & Athanassiou, A. Borrowing from nature: Biopolymers and biocomposites as smart wound care materials. *Front. Bioeng. Biotech.* **6**, 137 (2018).
2. Sahana, T. G. & Rekha, P. D. Biopolymers: Applications in wound healing and skin tissue engineering. *Mol. Biol. Rep.* **45**, 2857–2867 (2018).
3. Munoz-Bonilla, A., Echeverria, C., Sonseca, A., Arrieta, M. P. & Fernandez-Garcia, M. Bio-based polymers with antimicrobial properties towards sustainable development. *Materials* **12**, 641 (2019).
4. Mele, E. Electrospinning of natural polymers for advanced wound care: Towards responsive and adaptive dressings. *J. Mater. Chem. B* **4**, 4801–4812 (2016).
5. Smith, A. M., Moxon, S. & Morris, G. A. Biopolymers as wound healing materials. in *Wound Healing Biomaterials: vol. 2, Functional Biomaterials*, (ed. Agren, M. S.) 261–287 (Woodhead Publishing, London, 2016).
6. Bombaldi de Souza, R. F., Bombaldi de Souza, F. C., Bierhalz, A. C. K., Pires, A. L. R. & Moraes, A. M. Biopolymer-based films and membranes as wound dressings. in *Biopolymer Membranes and Films: Health, Food, Environment, and Energy Applications*, (ed. Agostini de Moraes, M., Ferreira da Silva, C. & Silveira Vieira R.) 165–194 (Elsevier, Amsterdam, 2020).
7. Homaeigohar, S. & Boccaccini, A. R. Antibacterial biohybrid nanofibers for wound dressings. *Acta Biomater.* **107**, 25–49 (2020).
8. Preda, N., Costas, A., Beregoi, M. & Enculescu, I. A straightforward route to obtain organic/inorganic hybrid network from bio-waste: Electroless deposition of ZnO nanostructures on eggshell membranes. *Chem. Phys. Lett.* **706**, 24–30 (2018).

9. Beregoi, M., Preda, N., Evangelidis, A., Costas, A. & Enculescu, I. Versatile actuators based on polypyrrole-coated metalized eggshell membranes. *ACS Sustain. Chem. Eng.* **6**, 10173–10181 (2018).
10. Preda, N., Costas, A., Enculescu, M. & Enculescu, I. Biomorphic 3D fibrous networks based on ZnO, CuO and ZnO–CuO composite nanostructures prepared from eggshell membranes. *Mater. Chem. Phys.* **240**, 122205 (2020).
11. Li, X., Ma, M., Ahn, D. U. & Huang, X. Preparation and characterization of novel eggshell membrane-chitosan blend films for potential wound-care dressing: From waste to medicinal products. *Int. J. Biol. Macromol.* **123**, 477–484 (2019).
12. Ahmed, T. A. E., Suso, H.-P. & Hincke, M. T. Processed eggshell membrane powder: Bioinspiration for an innovative wound healing product. *Mater. Sci. Eng. C* **95**, 192–203 (2019).
13. Liu, M. *et al.* Fabrication of KR-12 peptide-containing hyaluronic acid immobilized fibrous eggshell membrane effectively kills multi-drug-resistant bacteria, promotes angiogenesis and accelerates re-epithelialization. *Int. J. Nanomed.* **14**, 3345–3360 (2019).
14. Jung, J. Y. *et al.* Analysis of effect of eggshell membrane patching for moderate-to-large traumatic tympanic membrane perforation. *J. Audiol. Otol.* **21**, 39–43 (2017).
15. Guarderas, F., Leavell, Y., Sengupta, T., Zhukova, M. & Megraw, T. L. Assessment of chicken-egg membrane as a dressing for wound healing. *Adv. Skin Wound Care* **29**, 131–134 (2016).
16. Jun, H. J. *et al.* A new patch material for tympanic membrane perforation by trauma: the membrane of a hen egg shell. *Acta Oto-Laryngol.* **134**, 250–254 (2014).
17. Ray, P. G. *et al.* Sonication assisted hierarchical decoration of Ag-NP on zinc oxide nanoflower impregnated eggshell membrane: evaluation of antibacterial activity and in vitro cytocompatibility. *ACS Sustain. Chem. Eng.* **7**, 13717–13733 (2019).
18. Li, X., Cai, Z., Ahn, D. U. & Huang, X. Development of an antibacterial nanobiomaterial for wound-care based on the absorption of AgNPs on the eggshell membrane. *Colloid Surf. B-Biointerf.* **183**, 110449 (2019).
19. Liu, M. *et al.* Nano-silver-decorated microfibrillar eggshell membrane: Processing, cytotoxicity assessment and optimization, antibacterial activity and wound healing. *Sci. Rep.* **7**, 436 (2017).
20. Ohto-Fujita, E. *et al.* Solubilized eggshell membrane supplies a type III collagen-rich elastic dermal papilla. *Cell Tissue Res.* **376**, 123–135 (2019).
21. Vlad, V. Eggshell membrane separation method. US 2009/0306354A1.
22. DeVore, D. P. & Long, F. D. Anti-inflammatory activity of eggshell membrane and processed eggshell membrane preparations. US 2013/8580315B2.
23. Schmidt, R., Suso, H. P. & Kenny, E. Micronized eggshell membrane particles and the use thereof to promote the healing of wounds. US 2017/0319629A1.
24. Torres, F. G., Troncoso, O. P., Piaggio, F. & Hijar, A. Structure–property relationships of a biopolymer network: the eggshell membrane. *Acta Biomater.* **6**, 3687–3693 (2010).
25. Chen, L. & Peng, X. Silver nanoparticle decorated cellulose nanofibrous membrane with good antibacterial ability and high water permeability. *Appl. Mater. Today* **9**, 130–135 (2017).
26. Kung, M.-L. *et al.* Biomimetic polymer-based Ag nanocomposites as an antimicrobial platform. *Appl. Mater. Today* **4**, 31–39 (2016).
27. Babu, A. T. & Antony, R. Green synthesis of silver doped nano metal oxides of zinc and copper for antibacterial properties, adsorption, catalytic hydrogenation & photodegradation of aromatics. *J. Environ. Chem. Eng.* **7**, 102840 (2019).
28. Gupta, R., Eswar, N. K. R., Modak, J. M. & Madras, G. Ag and CuO impregnated on Fe doped ZnO for bacterial inactivation under visible light. *Catal. Today* **300**, 71–80 (2018).
29. Hong, D., Cao, G., Qu, J., Deng, Y. & Tang, J. Antibacterial activity of Cu₂O and Ag co-modified rice grains-like ZnO nanocomposites. *J. Mater. Sci. Technol.* **34**, 2359–2367 (2018).
30. Dadi, R., Azouani, R., Traore, M., Mielcarek, C. & Kanaev, A. Antibacterial activity of ZnO and CuO nanoparticles against gram positive and gram negative strains. *Mater. Sci. Eng. C* **104**, 109968 (2019).
31. Jan, T. *et al.* Superior antibacterial activity of ZnO–CuO nanocomposite synthesized by a chemical Co-precipitation approach. *Microb. Pathog.* **134**, 103579 (2019).
32. Wang, C. *et al.* Role of electric field and reactive oxygen species in enhancing antibacterial activity: A case study of 3D Cu foam electrode with branched CuO–ZnO NWs. *J. Phys. Chem. C* **122**, 26454–26463 (2018).
33. Wang, W. *et al.* Functionalization of polyvinyl alcohol composite film wrapped in a_m-ZnO@CuO@Au nanoparticles for antibacterial application and wound healing. *Appl. Mater. Today* **17**, 36–44 (2019).
34. Florica, C. *et al.* Superhydrophobic ZnO networks with high water adhesion. *Nanoscale Res. Lett.* **9**, 385 (2014).
35. Costas, A. *et al.* Radial heterojunction based on single ZnO–Cu_xO core-shell nanowire for photodetector applications. *Sci. Rep.* **9**, 5553 (2019).
36. Ahmad, M. & Zhu, J. ZnO based advanced functional nanostructures: Synthesis, properties and applications. *J. Mater. Chem.* **21**, 599–614 (2011).
37. Zoofakar, A. S., Rani, R. A., Morfa, A. J., O'Mullane, A. P. & Kalantar-zadeh, K. Nanostructured copper oxide semiconductors: A perspective on materials, synthesis methods and applications. *J. Mater. Chem. C* **2**, 5247–5270 (2014).
38. Girish Kumara, S. & Koteswara Rao, K. S. R. Zinc oxide based photocatalysis: Tailoring surface-bulk structure and related interfacial charge carrier dynamics for better environmental applications. *RSC Adv.* **5**, 3306–3351 (2015).
39. Saini, S. *et al.* Visible light induced α -amino acid synthesis from carbon dioxide using nanostructured ZnO/CuO heterojunction photocatalyst. *Materialia* **12**, 100777 (2020).
40. Pal, S., Maiti, S., Maiti, U. N. & Chattopadhyay, K. K. Low temperature solution processed ZnO/CuO heterojunction photocatalyst for visible light induced photo-degradation of organic pollutants. *CrystEngComm* **17**, 1464–1476 (2015).
41. Bera, S., Ghosh, S. & Basu, R. N. Fabrication of Bi₂S₃/ZnO heterostructures: An excellent photocatalyst for visible-light-driven hydrogen generation and photoelectrochemical properties. *New J. Chem.* **42**, 541–554 (2018).
42. Habibi-Yangjeh, A., Pirhashemi, M. & Ghosh, S. ZnO/ZnBi₂O₄ nanocomposites with p-n heterojunction as durable visible-light-activated photocatalysts for efficient removal of organic pollutants. *J. Alloy. Compd.* **826**, 154229 (2020).
43. Sabri, M., Habibi-Yangjeh, A. & Ghosh, S. Novel ZnO/CuBi₂O₄ heterostructures for persulfate-assisted photocatalytic degradation of dye contaminants under visible light. *J. Photochem. Photobiol. A-Chem.* **391**, 112397 (2020).
44. Rashid, J., Barakat, M. A., Salah, N. & Habib, S. S. ZnO-nanoparticles thin films synthesized by RF sputtering for photocatalytic degradation of 2-chlorophenol in synthetic wastewater. *J. Ind. Eng. Chem.* **23**, 134–139 (2015).
45. Ahumada-Lazo, R., Torres-Martinez, L. M., Ruiz-Gomez, M. A., Vega-Becerra, O. E. & Figueroa-Torres, M. Z. Photocatalytic efficiency of reusable ZnO thin films deposited by sputtering technique. *Appl. Surf. Sci.* **322**, 35–40 (2014).
46. Sardar, S. *et al.* Enhanced charge separation and FRET at heterojunctions between semiconductor nanoparticles and conducting polymer nanofibers for efficient solar light harvesting. *Sci. Rep.* **5**, 17313 (2015).
47. Ghosh, S., Remita, H. & Basu, R. N. Visible-light-induced reduction of Cr(VI) by PDPB-ZnO nanohybrids and its photo-electrochemical response. *Appl. Catal. B-Environ.* **239**, 362–372 (2018).
48. Ghosh, S., Amariei, G., Mosquera, M. E. G. & Rosal, R. Polymeric ruthenium precursor as a photoactivated antimicrobial agent. *J. Hazard. Mater.* **402**, 123788 (2021).
49. Kadavil, H., Zagho, M., Elzatahry, A. & Altahtamouni, T. Sputtering of electrospun polymer-based nanofibers for biomedical applications: A perspective. *Nanomaterials* **9**, 77 (2019).
50. Chuang, K.-T. *et al.* Metal oxide composite thin films made by magnetron sputtering for bactericidal application. *J. Photochem. Photobiol. A* **337**, 151–164 (2017).

51. Teodorescu, C. M., Esteva, J. M., Karnatak, R. C. & El Afif, A. An approximation of the Voigt I profile for the fitting of experimental X-ray absorption data. *Nucl. Instrum. Methods Phys. Res. A* **345**, 141–147 (1994).
52. Chauhan, I., Aggrawal, S. & Mohanty, P. ZnO nanowire-immobilized paper matrices for visible light-induced antibacterial activity against *Escherichia coli*. *Environ. Sci. Nano* **2**, 273–279 (2015).
53. Kaspar, T. C., Droubay, T., Chambers, S. A. & Bagus, P. S. Spectroscopic evidence for Ag(III) in highly oxidized silver films by X-ray photoelectron spectroscopy. *J. Phys. Chem. C* **114**, 21562–21571 (2010).
54. Liang, M. *et al.* Facile in situ synthesis of silver nanoparticles on procyanidin-grafted eggshell membrane and their catalytic properties. *ACS Appl. Mater. Interfaces* **6**, 4638–4649 (2014).
55. Zhu, L. *et al.* Synthesis of the 0D/3D CuO/ZnO heterojunction with enhanced photocatalytic activity. *J. Phys. Chem. C* **122**, 9531–9539 (2018).
56. Kelly, F. M. & Johnston, J. H. Colored and functional silver nanoparticle-wool fiber composites. *ACS Appl. Mater. Interfaces* **3**, 1083–1092 (2011).
57. Ding, Q. *et al.* Eggshell membrane-templated gold nanoparticles as a flexible SERS substrate for detection of thiabendazole. *Microchim. Acta* **186**, 453 (2019).
58. Matikainen, A. *et al.* Atmospheric oxidation and carbon contamination of silver and its effect on surface-enhanced Raman spectroscopy (SERS). *Sci. Rep.* **6**, 37192 (2016).
59. Zaier, M., Vidal, L., Hajjar-Garreau, S. & Balan, L. Generating highly reflective and conductive metal layers through a light-assisted synthesis and assembling of silver nanoparticles in a polymer matrix. *Sci. Rep.* **7**, 12410 (2017).
60. Dolatkah, A., Jani, P. & Wilson, L. D. Redox-responsive polymer template as an advanced multifunctional catalyst support for silver nanoparticles. *Langmuir* **34**, 10560–10568 (2018).
61. Battocchio, C. *et al.* Silver nanoparticles linked by Pt-containing organometallic dithiol bridge: Study on local structure and interface by XAFS and SR-XPS. *Phys. Chem. Chem. Phys.* **16**, 11719–11728 (2014).
62. Al-Hada, M. *et al.* Nanoparticle formation of deposited Ag_n-clusters on free-standing graphene. *Surf. Sci.* **665**, 108–113 (2017).
63. Shah, F. *et al.* Sonochemically synthesized green sorbent for the simultaneous removal of trace metal ions: application and estimation of measurement uncertainty through bottom-up approach. *New J. Chem.* **41**, 11695–11700 (2017).
64. Shao, C. *et al.* Eggshell membrane as a multimodal solid state platform for generating fluorescent metal nanoclusters. *J. Mater. Chem.* **21**, 2863–2866 (2011).
65. Liang, M. *et al.* Synthesis of well-dispersed Ag nanoparticles on eggshell membrane for catalytic reduction of 4-nitrophenol. *J. Mater. Sci.* **49**, 1639–1647 (2013).
66. Zaier, M., Vidal, L., Hajjar-Garreau, S., Bubendorff, J.-L. & Balan, L. Tuning the morphology of silver nanostructures photochemically coated on glass substrates: an effective approach to large-scale functional surfaces. *Nanotechnology* **28**, 105603 (2017).
67. Lee, S.-W. *et al.* Effect of temperature on the growth of silver nanoparticles using plasmon-mediated method under the irradiation of green LEDs. *Materials* **7**, 7781–7798 (2014).
68. Kelly, K. L., Coronado, E., Zhao, L. L. & Schatz, G. C. The optical properties of metal nanoparticles: The influence of size, shape, and dielectric environment. *J. Phys. Chem. B* **107**, 668–677 (2003).
69. Saleh, N. B. *et al.* Mechanistic lessons learned from studies of planktonic bacteria with metallic nanomaterials: implications for interactions between nanomaterials and biofilm bacteria. *Front. Microbiol.* **6**, 677 (2015).
70. Choi, O., Yu, C.-P., Fernandez, G. E. & Hu, Z. Interactions of nanosilver with *Escherichia coli* cells in planktonic and biofilm cultures. *Water Res.* **44**, 6095–6103 (2010).
71. Wang, Y. *et al.* Visible light driven type II heterostructures and their enhanced photocatalysis properties: A review. *Nanoscale* **5**, 8326–8339 (2013).
72. Jagadeeshan, S. & Parsanathan, R. Nano-metal oxides for antibacterial activity. in *Environmental Chemistry for a Sustainable World: Vol 25. Advanced Nanostructured Materials for Environmental Remediation*, (eds. Naushad, M., Rajendran, S. & Gracia, F.) 59–90 (Springer, Cham, 2019).
73. Varier, K. M. *et al.* Light-activated nanoparticles for antibacterial studies. in *Environmental Chemistry for a Sustainable World: Vol. 35. Green Methods for Wastewater Treatment*, (eds. Naushad, M., Rajendran, S. & Lichtfouse, E.) 73–86 (Springer, Cham, 2019).

Acknowledgements

This work was supported by the Core Program PN19-03 (contract no. 21 N/08.02.2019). A.C. acknowledges to PN-III-P1-1.1-PD-2019-1102 and M.B. acknowledges to PN-III-P1-1.1-PD-2019-1066.

Author contributions

N.P., A.C., M.B. and I.E. had the idea of the work and of the experiments steps. N.P. drafted the manuscript, A.C., M.B. and I.E. made the correction of the manuscript. N.P. performed the optical measurements and analyzed the XRD data. N.P., A.C. and M.B. carried out the RF magnetron sputtering deposition on ESMs. A.C. performed the FESEM and EDX measurements. N.A. obtained and analyzed the XPS data. A. K. made and analyzed the TEM investigations. C.C. and F.I. performed and analyzed the biological assessments. I.E. supervised the research, giving valuable advices about the whole experiments and manuscript. All authors read and approved the manuscript.

Competing interests

The authors declare no competing interests.

Additional information

Supplementary information is available for this paper at <https://doi.org/10.1038/s41598-020-78005-x>.

Correspondence and requests for materials should be addressed to N.P. or I.E.

Reprints and permissions information is available at www.nature.com/reprints.

Publisher's note Springer Nature remains neutral with regard to jurisdictional claims in published maps and institutional affiliations.



Open Access This article is licensed under a Creative Commons Attribution 4.0 International License, which permits use, sharing, adaptation, distribution and reproduction in any medium or format, as long as you give appropriate credit to the original author(s) and the source, provide a link to the Creative Commons licence, and indicate if changes were made. The images or other third party material in this article are included in the article's Creative Commons licence, unless indicated otherwise in a credit line to the material. If material is not included in the article's Creative Commons licence and your intended use is not permitted by statutory regulation or exceeds the permitted use, you will need to obtain permission directly from the copyright holder. To view a copy of this licence, visit <http://creativecommons.org/licenses/by/4.0/>.

© The Author(s) 2020